This is a previous version of the article published in Journal of Electroanalytical Chemistry. 2016, 763: 116-124. doi:10.1016/j.jelechem.2015.12.034

Ethanol oxidation on shape-controlled platinum nanoparticles at different pHs: a combined *in situ* IR spectroscopy and online mass spectrometry study

Carlos Busó-Rogero[a], *Sylvain Brimaud*[b], *Jose Solla-Gullon*[a], *Francisco J. Vidal-Iglesias*[a], *Enrique Herrero*[a], *R. Jürgen Behm* [b] *and Juan M. Feliu*[a]

[a] Instituto de Electroquímica, Universidad de Alicante Apartado 99, E–03080, Alicante, Spain

[b] Institut für Oberflächenchemie und Katalyse, Universität Ulm, Albert-Einstein-Allee 47, D-89081 Ulm, Germany

Abstract

Ethanol oxidation on different shape-controlled platinum nanoparticles at different pHs was studied using electrochemical, Attenuated Total Reflection – Fourier Transform Infrared Spectroscopy (ATR-FTIR) and, especially, Differential Electrochemical Mass Spectrometry (DEMS) techniques, which gives interesting quantitative information about the products of ethanol oxidation. Two Pt nanoparticle samples were used for this purpose: (100) and (111) preferentially oriented Pt nanoparticles. The results are in agreement with previous findings that the preferred decomposition product depends on surface structure, with CO_{ads} formation on (100) domains and acetaldehyde/acetic acid formation on (111) domains. However, new information has been obtained about the changes in CH_x and CO formation at lower potentials when the pH is changed, showing that CH_x formation is favored against the decrease in CO adsorption on (100) domains. At higher potentials, complete oxidation to CO_2 occurs from both CH_x and CO fragments. In (111) Pt nanoparticles, the splitting of C-C bond is hindered, favoring acetaldehyde and acetate formation even in 0.5 M H_2SO_4. C1 fragments become even less when the pH increases, being nearly negligible in the highest pH studied.

Keywords: Ethanol oxidation, pH effect, platinum, nanoparticles, DEMS

1. Introduction

During the last years, the search of new energy sources has been intensified due to the depletion of fossil fuels. In this sense, fuel cell technology has gained momentum for obtaining electric energy from the oxidation of a chemical fuel [1]. In the quest of possible new fuels, several options have been considered and particularly the oxidation of some small organic molecules such as formic acid, methanol or ethanol has been extensively evaluated. The oxidation of these molecules normally requires the use of platinum as catalyst [2-4]. Among these fuels, ethanol presents some relevant advantages to other fuels as i) it can be obtained directly from biomass and ii) it does not present problems for its storage. Unfortunately, and despite its high density energy for the complete oxidation to CO_2, with 12 electrons exchanged, problems dealing with a classical CO poisoning as well as to an incomplete oxidation to undesired products such as acetic acid, limit its potentialities for practical purposes.

Ethanol oxidation is also known to be a surface structure sensitive reaction, that is, the resulting catalytic activity depends on the particular/specific arrangement of the surface atoms. This surface structure sensitivity has been clearly evidenced by the use of Pt single crystal electrodes [5-7]. However, single crystal electrodes are ideal model surfaces which cannot be used in real electrocatalytic systems. For this reason, these results have to be extended to nanoparticles, which can be effectively applied such systems. As previously demonstrated, the effect of the particular arrangement of the atoms at the surface on the resulting ethanol oxidation activity is valid also for nanoparticles [8], thus highlighting the importance of gaining control of the surface structure of the nanoparticles to increase their electrocatalytic activity. Similar results on the effect of the surface structure of the nanoparticles for other important reactions such as oxygen reduction or other small organic molecule oxidations have been already reported [9-16]. In this sense, it is also worth noting that these shape/surface structure controlled Pt nanoparticles are usually about 8-10 nm in size which, from a practical point of view, may be

insufficient to fulfill the requirement of a high surface-to-volume ratio for practical applications.

From a mechanistic point of view, it is known that, in acidic solutions the reaction occurs via a complex reaction network. Scheme 1 illustrates a simplified mechanism where some additional steps such as desorption and re-adsorption of acetaldehyde have been not included for the sake of clarity.

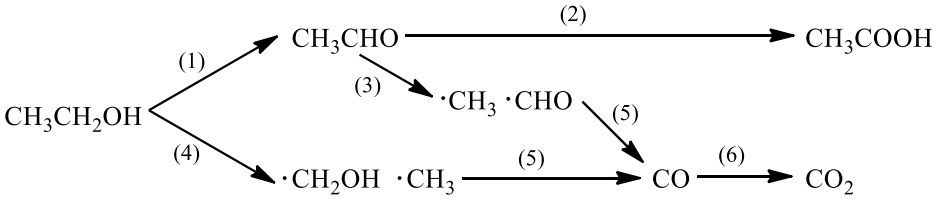

Reaction steps (1) and (2) give rise to the incomplete oxidation of ethanol, forming acetaldehyde and acetic acid as final products. To obtain this latter product, which is very difficult to oxidize, only four electrons are exchanged, thus wasting 2/3 of the formal energy density for ethanol. On Pt (111) electrodes and at room temperature, the reaction only takes places almost exclusively through this undesirable route [5]. On the other hand, the splitting of the C-C bond occurs in steps (3) and (4), which produce different carbon fragments that are subsequently transformed to CO_{ads} (step (5)) [17, 18]. Finally, in step (6), CO_{ads} is oxidized to CO_2, thus completing the 12 electron exchange route. This reaction route presents two difficult steps, i) the splitting of the C-C bond and ii) the oxidation of adsorbed CO. Pt(110) and especially Pt(100) electrodes favor the C-C bond scission, but suffer from surface poisoning. The enhancement of the C-C bond breaking rate needs to be accompanied by a higher rate for CO_{ads} oxidation to avoid poisoning. In fact, the stronger the metal-adsorbate bond, the more C-C bond breaking is favored, while CO_{ads} oxidation is disfavored. This is likely to result in a Sabatier type behavior with an optimum bond strength. In order to overcome this CO_{ads} poisoning problem, the incorporation of different foreign adatoms has been used to facilitate CO_{ads} oxidation to CO_2 [19-21]. In addition, the breakage of C-C bond is known to be improved

on Pt surfaces containing (100) and (110) steps on (111) terraces [6, 22]. Consequently, a combination of these two approaches, that is, using stepped Pt electrodes and foreign adatoms, gave rise to significant improvements in the oxidation reaction [17, 18].

On the other hand, the research of alkaline fuel cells (AFC) has currently grown due to the higher activity obtained at these pHs and also due to the their less corrosive properties, which favors the use of cheaper catalysts. In fact, the problems resulting from the carbonation of the system due to CO_2 retention as well as from the limited number of membranes capable of operating over long periods of time in alkaline media seem to be solved with the development of new anion-exchange membranes [23, 24]. According to fundamental studies performed in alkaline solutions [7, 25, 26], acetate is presented as the main product for ethanol oxidation regardless the surface structure of the Pt electrode, with negligible amounts of CO_{ads} being formed. Consequently, a better understanding of the changes in the oxidation mechanism as a function of the pH and in particular, how the ratio between the products (incomplete oxidation to acetate or complete oxidation towards CO_2) is modified for increasing pHs, would be of utmost interest.

To access this information, we have performed a combined *in situ* infrared (IR) spectroscopy and online mass spectrometry study on different shape controlled Pt nanoparticles of the ethanol oxidation reaction (EOR) at different pHs. These experiments will be performed under well-defined mass transport conditions and with control of the surface structure, in contrast to infrared reflection-absorption spectroscopy (IRRAS) measurements, where by-product accumulation, e.g. adsorbed acetate, is common. Such experimental conditions are more convenient for mechanistic investigations. On the other hand, it is also worth noting that only pHs lower than 4 have been explored in order to avoid problems due to carbonate formation. This combined approach allows us to not only perform a quantitative analysis of the volatile products formed during the reaction and to calculate the efficiencies for the complete

oxidation to CO_2, but also to follow the nature and potential window in which the adsorbed intermediate species are formed during the reaction.

2. Experimental

Two different kinds of Pt nanoparticles were used in this work. They were both synthesized using a colloidal method [27, 28], and displayed preferential (100) or (111) surface orientations. These nanoparticles were denoted as (100) Pt nanoparticles and (111) Pt nanoparticles, depending on their dominant surface structure. Experimental details about the synthesis, also including Transmission Electron Microscopy (TEM) characterization to determine their particle size and characterize their preferential shape, were previously described [29]. Very briefly, the predominant shape was cubic for (100) Pt nanoparticles and octahedral for (111) ones. The particle size of both nanoparticles batches was estimated to be about 8-10 nm. The electrodes were prepared by depositing a droplet (4 μL) of the aqueous solution containing the nanoparticles on a hemispherical gold substrate, after which the electrode was protected under an Ar stream until complete solvent evaporation. Before the measurements, Pt nanoparticles were carefully cleaned by CO adsorption and subsequent stripping at potentials below 0.95 V to preserve the surface structure of the samples. The electrochemically active area of Pt nanoparticles was measured using the charge involved in the so-called hydrogen/anion adsorption/desorption region (between 0.05 V and 0.6 V) from the cyclic voltammograms recorded in 0.5 M H_2SO_4, assuming that the charge density for this region is 230 μC cm^{-2} in sulfuric acid solutions [30].

IR spectroelectrochemical probing of adsorbates and online detection of volatile reaction products were performed simultaneously using a dual thin-layer spectroelectrochemical flow-cell in which ATR-FTIR and DEMS measurements can be carried put. A more detailed description of this flow-cell configuration was previously given in [31]. In brief, the central cell

is a double thin-layer flow cell, equipped with two Pt counter electrodes (a Pt gauge and a Pt wire) at the inlet and the outlet of flow cell. For electrolyte changing, two electrolyte reservoirs are available, one with the supporting electrolyte alone and one with ethanol + supporting electrolyte. The working electrode is prepared by depositing the nanoparticles on a Au film covering a Si wafer, which in turn is coupled with the flat side of a hemispherical Si prism. The Au film was prepared by electroless deposition following the procedure reported previously [32-34]. It has to be thin enough to allow the IR radiation to pass to the nanoparticles, but thick enough to be sufficiently conductive for obtaining a good electrochemical response.

In the first thin-layer compartment, the flat side of the prism was pressed via a circular tightening gasket and a Cu foil current collector against the Kel-F body of the cell, forming a thin electrolyte layer with a volume of ca. 10 μL. The electrolyte flows to the second thin-layer compartment through six capillaries. The second thin-layer compartment is connected via a porous Teflon membrane to a mass spectrometer, such that gaseous species can pass through and be detected on-line.

The *in situ* ATR-FTIRS experiments were performed in a BioRad FTS-6000 spectrometer equipped with a homemade reflection accessory (incident angle of 70º) and mercury cadmium telluride (MCT) detector. The resolution and the acquisition time per spectra were 4 cm^{-1} and 10 s, respectively. The spectra are presented in absorbance values, as the ratio $-\log R/R_0$, where R and R_0 are the reflectance values corresponding with the single beam spectra measured at the sample or reference potential, respectively. Negative bands in the spectra correspond with species formed at the sampling potential, whereas positive bands indicate a consumption of the species with respect to reference potential.

The DEMS setup is explained in detail in ref. [35]. Briefly, it is based on a differentially pumped two-chamber system coupled with a Balzers QMS 12 quadrople mass spectrometer, a Pine Instruments potentiostat and a computerized data acquisition system. In all the mass

spectrometry experiments, large Pt loadings were used to favor the performance of DEMS experiments.

The calibration constant for CO_2 was determined by passing a CO saturated solution at 0.1 V until the Pt surface is completely blocked. Then, the electrolyte is changed to CO-free supporting electrolyte for 15 min, to assure the complete removal of dissolved CO in the thin-layer cell. After that, a CO_{ads} stripping experiment was carried out. The calibration constant K* was calculated by comparison of the Faradaic oxidation current and the CO_2 mass signal, using the following equation [36]:

$$K^* = z\frac{Q_{MS}}{Q_F} \qquad (1)$$

where z is the number of electrons exchanged in the CO oxidation reaction to CO_2, Q_{MS} is the integrated charge of the mass current for the CO_2 spectrometric signal (*m/z*=44) and Q_F is the integrated Faradaic current charge in the CO_{ad} stripping peak.

To eliminate contributions from acetaldehyde species to the mass signal *m/z*=44 for calculating the CO_2 current efficiency in the ethanol oxidation reaction, the following equation was used:

$$I_{MS}(CO_2) = I(m/z = 44) - n * I(m/z = 29) \qquad (2)$$

where *n* is a parameter determined from the ratio between the stable I_{44} and I_{29} currents in the oxidation transients at 0.9 V at each pH, and assuming that the efficiency for acetaldehyde production at this potential is 100%, as has been observed previously [36]. The values obtained for *n* are always between 0.60 and 0.65. To convert this CO_2 mass current to the Faradaic current, the calibration constant *K** was used:

$$I_F(CO_2) = z\frac{I_{MS}(CO_2)}{K^*} \qquad (3)$$

For this expression, *z* is equal to 6, the number of electrons exchanged per C atom for complete CO_2 oxidation. Finally, the CO_2 current efficiency is the ratio between CO_2 and total Faradaic currents:

$$A_{CO_2} = \frac{I_F(CO_2)}{I_F} \qquad (4)$$

All experiments were carried out at room temperature. Millipore Milli Q water (18.2 MΩ cm), H_2SO_4 (Suprapur, Merck), Na_2SO_4 (HiPerSolv, Prolabo) and ethanol absolute (Merck p.a.) were used to prepare the solutions. Solutions of different pH were obtained by adding some droplets of H_2SO_4 to 0.5 M SO_4^{2-} solutions until the desired pH value was reached. The sulfate concentration was kept at approximately 0.5 M for all experiments. Solutions were deaerated with N_2/Ar, and CO (Messer-Griesheim, N 4.7) was used to saturate the supporting electrolyte solution used for cleaning the nanoparticles and for calibrating the DEMS signals. A Saturated Calomel Electrode (SCE) served as a reference during the simultaneous ATR-FTIRS/DEMS experiments, but all the potentials presented in this paper are referred to that of the reversible hydrogen electrode (RHE).

3. Results and discussion

3.1 Electrochemical characterization

Fig. 1 shows the characteristic cyclic voltammetric profiles in 0.5 M H_2SO_4 for the Pt nanoparticles used in this work. Both cyclic voltammograms (CVs) show symmetric voltammetric peaks, which is an indication of the surface cleanness. The resulting voltammetric profiles can be considered as a fingerprint of each Pt nanoparticle sample and allow a detailed evaluation of the specific surface structure [29]. As previously shown, the main features are those related to the presence of large (100) ordered domains (signal at about 0.37 V) due to the hydrogen adsorption/desorption process and those associated with the sulfate adsorption on (111) ordered domains (signal about 0.5 V) [29]. As expected, cubic Pt nanoparticles displayed

the characteristic feature of the wide (100) domains while for octahedral ones the CV was dominated by the characteristic features coming from the (111) ordered domains. A more detailed analysis about the correlations between shape, surface structure and resulting voltammetric profiles has been done previously in our group [12, 29, 30].

3.2 Ethanol oxidation at low pHs

The voltammetric responses for ethanol oxidation (1st scan) obtained with the different Pt nanoparticles in 0.05 M EtOH + 0.5 M SO_4^{2-} at two different pH values are displayed in Fig. 2. As previously mentioned, the upper potential limit is limited to 0.95 V in order to avoid significant changes of the Pt surfaces due to oxide formation/reduction processes. Also, and in comparison with previous works [7, 8], the ethanol concentration is lowered to prevent problems with membrane saturation in the DEMS experiments. As mentioned before, experiments were carried out at pH values below 4 to avoid carbonate formation from the reaction of CO_2 with water, which can mask the CO_2 efficiency. On the other hand, the surface area of the nanoparticles was kept relatively low (0.03-0.05 cm^2 of active area) to ensure that the entire deposit is contributing to the oxidation reaction. In this sense, it is worth noting that the use of high metal loadings and consequently high surface areas creates nanostructured electrodes in which only the outer part of the deposit is effectively working, due to a poor diffusion of ethanol to the inner parts, giving rise to lower than expected current densities [37].

In the positive-going sweep and at potentials below *ca.* 0.4 V, the voltammetric profiles present low currents due to the formation of CO_{ads}, which blocks the active surface. As has been shown, this process takes place even at potentials as low as 0.1 V [17, 18], and CO_{ads} is accumulated on the surface since it is not effectively oxidized at room temperature at E<0.6 V. As the potential is increased, CO_{ads} is oxidized and the current increases until an oxidation peak at around 0.8 V is observed. From this point, ethanol oxidation is hindered by adsorbed species

(anions present in solution or OH^-) and/or by the incipient oxide formation. In the negative-going sweep and after the reactivation of the surface, currents are higher than those measured in the positive-going scan, since the surface is now free from CO_{ads} and for E>0.6 V, the possible CO_{ads} formed in the process is immediately oxidized. This leads to a hysteresis between both scan directions, which is proportional to the amount of CO_{ads} formed at low potentials. The decrease at E<0.6 V is a consequence of the CO_{ads} re-poisoning of the surface and the diminution of oxidation rates as the electrode potential diminishes [38, 39]. However, this process depends on the surface structure and on the pH of the electrolyte. At pH=0.3, (100) Pt nanoparticles (Fig. 2a) present a more prominent peak at 0.8 V, which is a characteristic of (100) surfaces. As it has been previously shown in single crystal electrode studies, Pt(100) is more active for the formation of CO than the Pt(111) electrode, leading to a complete blockage of the surface at low potentials [5]. The subsequent oxidation of CO with the concomitant reactivation of the surface gives rise to the peak at 0.8 V on the Pt(100) electrode [5, 8]. This preference for CO formation at low potentials is also the cause of a more pronounced hysteresis between positive and negative-going sweeps for the (100) Pt nanoparticles than for the (111) Pt ones. However, by increasing the pH, this hysteresis decreases for both nanoparticle samples, probably due to a lower CO_{ads} formation rate, as will be shown later. In terms of maximum current densities, (100) Pt nanoparticles (Fig. 2a) display a similar peak current density for the two pH values, which means that, despite different CO formation and probably different CO_2 current efficiencies, the overall activity for the reaction, under non-stationary conditions, is maintained. On the other hand, (111) Pt nanoparticles (Fig. 2b) show a lower hysteresis and higher peak current as the pH increases, suggesting that cleavage of the C-C bond is disfavored and acetaldehyde/acetic acid products are preferred instead of CO_2 formation. This fact seems to be in good agreement with what was observed for surfaces with large (111) ordered domains in strongly alkaline solutions [7, 40], where only the incomplete oxidation is achieved and no

adsorbed CO is detected in the whole potential range. This discussion will be continued in the next sections with data obtained from DEMS experiments.

To evaluate the adsorbed species present on the Pt surface during ethanol oxidation at these pHs, FTIR experiments were carried out. Fig. 3 displays ATR measurements at 0.4 V vs RHE, using spectra taken at 0.9 V, where CO is completely oxidized to CO_2, as reference spectra. All spectra were recorded under almost stationary conditions. At 0.4 V, the fragments formed from ethanol oxidation poison the active surface.

In the IR experiments, the main band observed corresponds to linearly adsorbed CO in the spectral range between 2030 and 2070 cm^{-1}. In the two samples studied, (100) Pt and (111) Pt nanoparticles (Fig. 3a and 3b respectively), the CO bands diminish with increasing pH, as it was predicted from the hysteresis in the voltammetric experiments. Comparing the two experiments, it seems that the CO bands are higher for (100) domains than for (111) sites, although, in agreement with our previous findings [8]. Unfortunately, a direct comparison is not simple due to the different experimental conditions for each electrode. Additionally, no band of adsorbed acetate can be detected, in contrast with previous results [8]. This absence of the adsorbed acetate band is due to the fact that these experiments are performed under flow cell conditions, where the acetic acid formed in the reaction is readily removed from the vicinity of the electrode, thus preventing its adsorption as weakly bound acetate. Thus, in this way, its accumulation on the surface is minimized, thus allowing a better approach to the understanding of the reaction mechanism.

3.3 DEMS experiments

For obtaining new quantitative data about the formation of acetate, CO_2, CH_x or other intermediates or products during ethanol oxidation, DEMS experiments were carried out. Fig. 4 and Fig. 5 display cyclic voltammetric experiments and the corresponding mass spectrometric currents (m/z=44 and m/z=29) obtained at different pH values using (100) Pt and (111) Pt

nanoparticles, respectively. The scan rate used during the experiments was 5 mV s^{-1} and the flow rate was around 10 μL s^{-1}. In the figures, the 2nd cycle in DEMS experiments is presented, because this profile is a very good approximation to the steady-state behavior. As described in the experimental section, the m/z=44 current includes contributions from acetaldehyde (CH_3CHO^+) and CO_2, whereas the m/z=29 signal only includes contributions from the acetaldehyde (CHO^+) fragment.

In the case of (100) Pt nanoparticles (Fig. 4), the shape of the mass spectrometric voltammogram for I_{29} is similar to that observed for the Faradaic current, which suggests that ethanol oxidation proceeds mainly via acetaldehyde formation. However, the I_{44} mass spectrometric voltammogram shows some slight differences in the region at 0.7-0.8 V, probably due to the formation of CO_2 from the oxidation of CO_{ads} generated at lower potentials. On the other hand, for (111) Pt nanoparticles (Fig. 5), the shape of the I_{29} and I_{44} mass spectrometric voltammograms are almost identical, confirming that CO_{ads} formation/CO_{ads} oxidation are less than in the previous case. For both nanoparticle samples, I_{29} and I_{44} come only from acetaldehyde formation at higher potentials than 0.9 V, where CO_{ads} formed at lower potentials has been completely oxidized to CO_2 [36]. Considering the current peaks in the mass spectrometric signals for the negative-going potential scan, the ratio between I_{44} and I_{29} is around 60%, independent of the pH or the Pt sample. This is the same relative intensity as obtained in the steady-state oxidation process at 0.9 V. This ratio will be used later for calculating the CO_2 efficiency. Comparing the peak potentials measured for the three different pH values studied, the peak potential is shifted positively with increasing pH for (100) Pt nanoparticles, while for the (111) nanoparticles no significant change is observed. Since the peak for the (100) nanoparticles is mainly related to the oxidation of the adsorbed CO, this would mean that CO_{ads} oxidation is shifted toward more positive values as the pH increases due

to the different CO_{ads} coverages observed in this sample. This effect is not observed for (111) Pt nanoparticles, presumably due to the lower amount of CO_{ads} formed at low potentials [5, 22].

Fig. 6 displays CO_2 Faradaic currents for the two samples studied during this work, calculated using eqs. (2), (3) and (4). The data used to calculate these currents were obtained from fig. 4 and fig. 5. These experiments were done to clarify the preference of (100) sites for complete oxidation as compared to (111) domains. The shape of the CO_2 Faradaic current vs. E curve is similar to the voltammogram measured during a CO_{ads} stripping experiment, showing a peak at around 0.7 V vs RHE, which corresponds to the oxidation of adsorbed CO to CO_2. The shape of this CO_2 current trace agrees well with previous findings [41]. Also, the peak potential for the CO_2 Faradaic current shifts toward higher values with increasing pH, especially for the (100) Pt nanoparticles, corroborating that the peak potential shift in the voltammogram is mainly related to the oxidation of adsorbed CO. The absence of currents in the negative scan direction clearly indicates that the cleavage of the C-C bond occurs only at low potentials, below 0.5 V. At those potentials, the cleavage produces adsorbed CO, which is only oxidized in the subsequent positive-going scan at higher potentials. If the cleavage of the C-C bond had taken place at high potentials, some Faradaic current for CO_2 formation would have been detected in the negative scan direction.

In order to better compare the CO_2 efficiency of the two samples, the calculated current efficiencies for CO_2 at pH=0.3 are displayed in Fig. 7 for the positive scan direction. Maximum CO_2 current efficiencies for the (100) Pt nanoparticles (ca. 10 %) are almost double of those measured for the (111) Pt nanoparticles (ca. 5 %), corroborating the voltammetric results. Maximum efficiencies are obtained at ca. 0.65 V for both samples. This potential is lower than the peak potential for the Faradaic CO_2 current, due to the competition between the oxidation of ethanol to acetaldehyde and acetic acid and that of adsorbed CO. As the CO_{ads} stripping process takes place, ethanol oxidation current becomes higher due to the potential increase and

also due to the rise in the number of free sites on the surface, where the partial oxidation of ethanol can occur. It should be highlighted that both curves have a very similar shape, indicating that the same type of sites are active for the C-C bond cleavage on both samples. The only difference between them is their relative number on the samples.

3.4 Ethanol stripping experiments

From the FTIR-DEMS results it is clear that the cleavage of the C-C bond is the key process to achieve the complete oxidation of ethanol [22, 42]. This process takes place at potentials below 0.4 V. Results with single crystal electrodes have shown that once the C-C bond is broken, the carbon containing the alcohol group immediately evolves to give adsorbed CO, whereas the CH_x fragment only yields adsorbed CO at E>0.4-0.5 V [17, 18]. To obtain additional information on this process, ethanol stripping experiments were done. In this experiment, an ethanol solution is flown through the cell at 0.4 V for two minutes, to allow the cleavage of ethanol molecules and adsorption of fragments. After that, the solution is changed to a solution containing only the supporting electrolyte at the same pH and then the electrode is cycled between 0.04 and 0.95 V vs RHE at v=5 mVs^{-1}, registering simultaneously the Faradic and mass spectrometric ion currents [39, 43].

Fig. 8 displays ethanol stripping experiments for the (100) Pt nanoparticles, studying ion currents m/z=15 and m/z=44. I_{15} provides information about the CH_x fragment in its reduction to CH_4 at low potentials [36, 44] whereas I_{44} in this particular case only gives information about CO_2 formed, since ethanol has been removed from the solution. Some authors have also evaluated the mass current m/z=61, which corresponds to a fragment of ethyl acetate ($CH_3COOH_2^+$), to follow the acetic acid formation, whose volatility is low and cannot be detected in DEMS experiments [45, 46]. However, as shown in these papers, the intensity of this mass current signal is very low and, consequently, it was not measured in the present

contribution. Fig. 8a shows the voltammetric profile after ethanol adsorption for (100) Pt nanoparticles. As expected, in the 1st cycle, active sites of platinum nanoparticles are blocked due to CO_{ads} formation. At higher potentials, CO_{ads} is oxidized to CO_2 and the voltammogram recovers the characteristic features of the (100) nanoparticles in the so-called hydrogen region. Fig. 8b shows mass currents at m/z=15 simultaneously recorded with the voltammogram. At low potentials (around 0.1 V), a small peak is detected due to CH_4 formation from the reduction of the CH_x fragment. This signal increases with the pH. At higher potentials, adsorbed CO is oxidized to CO_2, as it can be seen in Fig. 8c. For this type of nanoparticles, I_{44} peak does not significantly change with the pH.

Fig. 9 shows the same experiments as done in Fig. 8, but using (111) Pt nanoparticles. From the evolution of the I_{15} and I_{44} currents with the pH it can be seen that both signals decrease significantly with pH. In order to quantitatively analyze the results of both samples, the normalized charges under mass signals m/z=15 and m/z=44 have been calculated (Fig. 10). As stated before, at 0.4 V, ethanol molecules can dissociate, giving rise to two single carbon containing fragments, the one containing the oxygen group, which immediately reacts to adsorbed CO, and the CH_x fragment, which is more difficult to oxidize to form adsorbed CO. The CH_x fragment can also interact with the surface and be reduced at low potentials. Depending on the cleavage rate and the rate for the oxidation of the CH_x fragment to CO_{ads}. and how these rates evolve with the pH, several situations can be found. For the (100) Pt nanoparticles, the amount of CO_{ads} is independent of the pH, which indicates that the CO_{ads} coverage has reached a value where further C-C bond cleavage is fully inhibited. Probably only isolated sites remain free and, on those sites, this process cannot take place. This means that the C-C bond cleavage is fast enough to produce a saturated adlayer of CO during the time (2 min.) at 0.4 V. Since the oxidation of the CH_x fragment is very slow at 0.4 V, the increase of the signal for CH_4 production as the pH increases indicates that the oxidation of this fragment to

yield adsorbed CO is even slower. At lower pHs, the saturated CO adlayer formed contains a higher fraction of CO_{ads} molecules coming from the CH_x fragment and for this reason the signal is small. As the pH increases, the oxidation rate of this fragment to CO_{ads} diminishes at a higher rate than that of the C-C bond cleavage, resulting in a higher number of unreacted CH_x fragments on the electrode surface, thus producing a higher current for CH_4 production.

On the other hand, for the (111) Pt nanoparticles, the rate for the C-C cleavage is slower, because of the lower fraction of (100) sites on the sample. Thus, lower CO coverages are obtained as revealed in Fig. 10. These coverages are below the saturation value. On the other hand, the charge for CH_4 production at pH=0.3 is similar to that measured for the (100) Pt nanoparticles, which indicates that also the oxidation rate of CH_x to CO is low for these nanoparticles. As the pH increases, C-C bond cleavage rate diminishes, resulting in lower CO_{ads} coverages and lower CH_4 formation. The diminution in the CH_4 signal is proportionally smaller than that of the CO_2 due to a two effects. The C-C bond cleavage rate is slower but also the transformation of the CH_x fragment to CO, resulting in a compensating effect in which the diminution of unreacted CH_x fragments is smaller. The lower reactivity of surfaces for the cleavage of the C-C bond as the pH increases is in agreement with the results obtained in alkaline medium. In the latter environment, only acetate bands are detected in FTIR experiments for ethanol oxidation [7]. Bands related to $CH_{x,ads}$ have only been seen in wide (111) ordered domains by SERS in these media [25], whereas these bands were not detected in the case of Pt polyoriented surfaces [47], in agreement with our results.

4. Conclusions

Ethanol oxidation experiments with Pt nanoparticles were performed using voltammetric, ATR and DEMS experiments, studying the acidic pH range below 4 to avoid carbonate formation and using always 0.5 M SO_4^{2-} to discard anion effects. As a summary of the data

obtained, the next scheme shows the preferred path for each site taking into account the pH effect in acidic solutions:

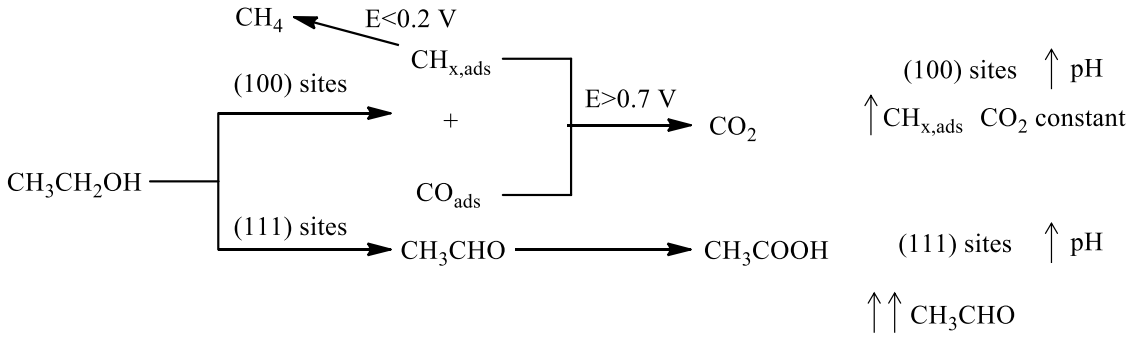

The results presented clearly show structure effects related to the (100) and (111) domains, in agreement with studies done with single crystal electrodes. In spite of the fact that the incomplete ethanol oxidation was established as the preferred route for both samples, a higher activity for the formation of C1-fragments (CO_{ads}, $CH_{x,ads}$) as intermediates was observed for (100) domains. The maximum CO_2 efficiency calculated from DEMS data corroborated this behavior, as it is higher for (100) nanoparticles (around 10%) than for (111) nanoparticles (around 5%). When the pH is increased, $CH_{x,ads}$ was also detected, in addition to CO_{ads}. $CH_{x,ads}$ formation is favored at lower potentials on preferentially oriented (100) Pt nanoparticles and decreasing CO formation. For (111) Pt nanoparticles, CO_{ads} formation is hindered and also the splitting of the C-C bond, promoting acetaldehyde/acetic acid formation up to quasi-negligible CO_2 formation at higher pHs.

Acknowledgements

This work has been financially supported by the MCINN-FEDER (Spain) and Generalitat Valenciana through projects CTQ 2013-44083-P and PROMETEO/2014/013, respectively.

References

[1] M.T.M. Koper, Fuel Cell Catalysis: A Surface Science Approach, John Wiley & Sons, Hoboken, New Jersey, 2009.
[2] C. Rice, R.I. Ha, R.I. Masel, P. Waszczuk, A. Wieckowski, T. Barnard, J. Power Sources, 111 (2002) 83.
[3] T. Iwasita, Electrochim. Acta, 47 (2002) 3663.
[4] E. Antolini, J. Power Sources, 170 (2007) 1.
[5] F. Colmati, G. Tremiliosi-Filho, E.R. Gonzalez, A. Berna, E. Herrero, J.M. Feliu, Faraday Discuss., 140 (2008) 379.
[6] F. Colmati, G. Tremiliosi, E.R. Gonzalez, A. Berna, E. Herrero, J.M. Feliu, Phys. Chem. Chem. Phys., 11 (2009) 9114.
[7] C. Busó-Rogero, E. Herrero, J.M. Feliu, ChemPhysChem, 15 (2014) 2019.
[8] C. Buso-Rogero, V. Grozovski, F.J. Vidal-Iglesias, J. Solla-Gullon, E. Herrero, J.M. Feliu, J. Mater. Chem. A, 1 (2013) 7068.
[9] J. Hernández, E. Herrero, J. Solla-Gullón, F.J. Vidal-Iglesias, J.M. Feliu, A. Aldaz, Shape-dependent electrocatalysis: Oxygen reduction on gold nanoparticles, in, vol. PV 2005-11, 2005, pp. 200.
[10] J. Solla-Gullón, F.J. Vidal-Iglesias, A. López-Cudero, E. Garnier, J.M. Feliu, A. Aldaz, Phys. Chem. Chem. Phys., 10 (2008) 3689.
[11] F.J. Vidal-Iglesias, J. Solla-Gullón, V. Montiel, J.M. Feliu, A. Aldaz, J. Phys. Chem. B, 109 (2005) 12914.
[12] V. Grozovski, J. Solla-Gullon, V. Climent, E. Herrero, J.M. Feliu, J. Phys. Chem. C, 114 (2010) 13802.
[13] F.J. Vidal-Iglesias, R.M. Aran-Ais, J. Solla-Gullon, E. Garnier, E. Herrero, A. Aldaz, J.M. Feliu, Phys. Chem. Chem. Phys., 14 (2012) 10258.
[14] F.J. Vidal-Iglesias, J. Solla-Gullon, E. Herrero, A. Aldaz, J.M. Feliu, Angew. Chem. Int. Ed., 49 (2010) 6998.
[15] F.J. Vidal-Iglesias, J. Solla-Gullón, A. Rodes, E. Herrero, A. Aldaz, J. Chem. Educ., 89 (2012) 936.
[16] C. Buso-Rogero, J.V. Perales-Rondon, M.J.S. Farias, F.J. Vidal-Iglesias, J. Solla-Gullon, E. Herrero, J.M. Feliu, Phys. Chem. Chem. Phys., 16 (2014) 13616.
[17] J. Souza-Garcia, E. Herrero, J.M. Feliu, ChemPhysChem, 11 (2010) 1391.
[18] V. Del Colle, J. Souza-Garcia, G. Tremiliosi, E. Herrero, J.M. Feliu, Phys. Chem. Chem. Phys., 13 (2011) 12163.
[19] C. Lamy, S. Rousseau, E.M. Belgsir, C. Coutanceau, J.M. Leger, Electrochim. Acta, 49 (2004) 3901.
[20] V. Del Colle, A. Berna, G. Tremiliosi, E. Herrero, J.M. Feliu, Phys. Chem. Chem. Phys., 10 (2008) 3766.
[21] J.P.I. de Souza, S.L. Queiroz, K. Bergamaski, E.R. Gonzalez, F.C. Nart, J. Phys. Chem. B, 106 (2002) 9825.
[22] S.C.S. Lai, M.T.M. Koper, Faraday Discuss., 140 (2008) 399.
[23] J.R. Varcoe, R.C.T. Slade, E.L.H. Yee, S.D. Poynton, D.J. Driscoll, D.C. Apperley, Chem. Mater., 19 (2007) 2686.
[24] C. Coutanceau, L. Demarconnay, C. Lamy, J.M. Leger, J. Power Sources, 156 (2006) 14.
[25] S.C.S. Lai, M.T.M. Koper, Phys. Chem. Chem. Phys., 11 (2009) 10446.
[26] P.A. Christensen, S.W.M. Jones, A. Hamnett, J. Phys. Chem. C, 116 (2012) 24681.

[27] T.S. Ahmadi, Z.L. Wang, T.C. Green, A. Henglein, M.A. El-Sayed, Science, 272 (1996) 1924.
[28] T.S. Ahmadi, Z.L. Wang, A. Henglein, M.A. El-Sayed, Chem. Mater., 8 (1996) 1161.
[29] J. Solla-Gullón, P. Rodríguez, E. Herrero, A. Aldaz, J.M. Feliu, Phys. Chem. Chem. Phys., 10 (2008) 1359.
[30] Q.S. Chen, J. Solla-Gullon, S.G. Sun, J.M. Feliu, Electrochim. Acta, 55 (2010) 7982.
[31] M. Heinen, Y.X. Chen, Z. Jusys, R.J. Behm, Electrochim. Acta, 52 (2007) 5634.
[32] S. Brimaud, Z. Jusys, R.J. Behm, Beilstein J Nanotech, 5 (2014) 735.
[33] H. Miyake, S. Ye, M. Osawa, Electrochem. Commun., 4 (2002) 973.
[34] S. Brimaud, Z. Jusys, R.J. Behm, Electrocatalysis, 2 (2011) 69.
[35] Z. Jusys, R.J. Behm, J. Phys. Chem. B, 105 (2001) 10874.
[36] A.A. Abd-El-Latif, E. Mostafa, S. Huxter, G. Attard, H. Baltruschat, Electrochim. Acta, 55 (2010) 7951.
[37] S. Chumillas, C. Busó-Rogero, J. Solla-Gullón, F.J. Vidal-Iglesias, E. Herrero, J.M. Feliu, Electrochem. Commun., 13 (2011) 1194.
[38] H. Wang, Z. Jusys, R.J. Behm, J. Phys. Chem. B, 108 (2004) 19413.
[39] E. Mostafa, A.A. Abd-El-Latif, R. Ilsley, G. Attard, H. Baltruschat, Phys. Chem. Chem. Phys., 14 (2012) 16115.
[40] C. Busó-Rogero, J. Solla-Gullón, F. Vidal-Iglesias, E. Herrero, J. Feliu, J. Solid State Electrochem., (2015) 1.
[41] J.F. Gomes, D. Profeti, L.J. Deiner, ChemElectroChem, 1 (2014) 655.
[42] C. Lamy, C. Coutanceau, in: Z.-X.L.a.T.S. Zhao (Ed.) Catalysts for Alcohol-Fuelled Direct Oxidation Fuel Cells, vol. 6, RSC Energy and Enviroment Series 2012, Ch. 1.
[43] M. Heinen, Z. Jusys, R.J. Behm, J. Phys. Chem. C, 114 (2010) 9850.
[44] T. Iwasita, E. Pastor, Electrochim. Acta, 39 (1994) 531.
[45] T. Herranz, M. Ibanez, J.L.G. de la Fuente, F.J. Perez-Alonso, M.A. Pena, A. Cabot, S. Rojas, ChemElectroChem, 1 (2014) 885.
[46] S.C.S. Lai, M.T.M. Koper, Journal of Physical Chemistry Letters, 1 (2010) 1122.
[47] S.C.S. Lai, S.E.F. Kleijn, F.T.Z. Öztürk, V.C. van Rees Vellinga, J. Koning, P. Rodriguez, M.T.M. Koper, Catal. Today, 154 (2010) 92.

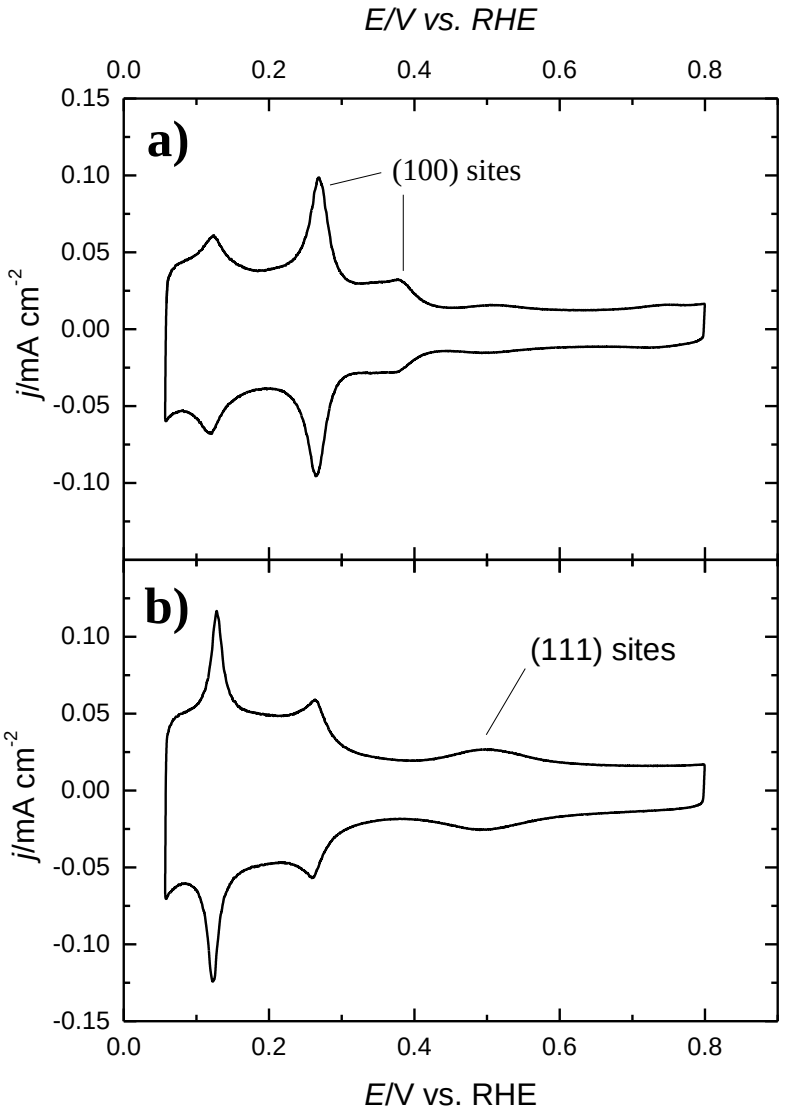

Figure 1. Voltammetric profiles corresponding to a) (100) Pt and b) (111) Pt nanoparticles in 0.5 M H_2SO_4. Scan rate: 0.05 V s^{-1}.

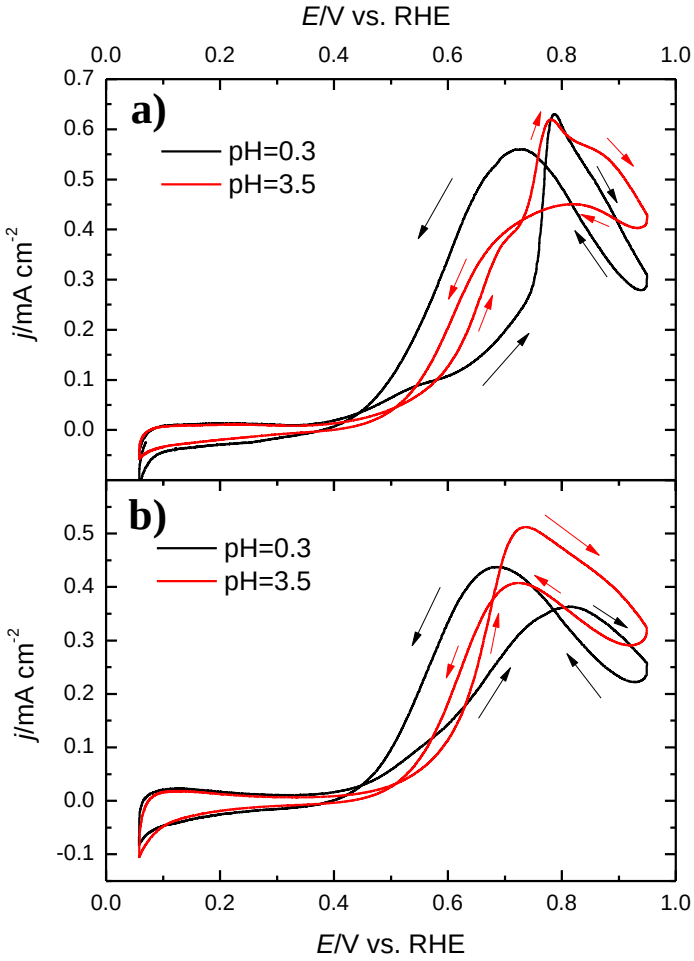

Figure 2. Voltammetric profiles for a) (100) Pt and b) (111) Pt nanoparticles in 0.05 M CH_3CH_2OH + 0.5 M SO_4^{2-} at different pHs. Scan rate: 0.02 V s^{-1}.

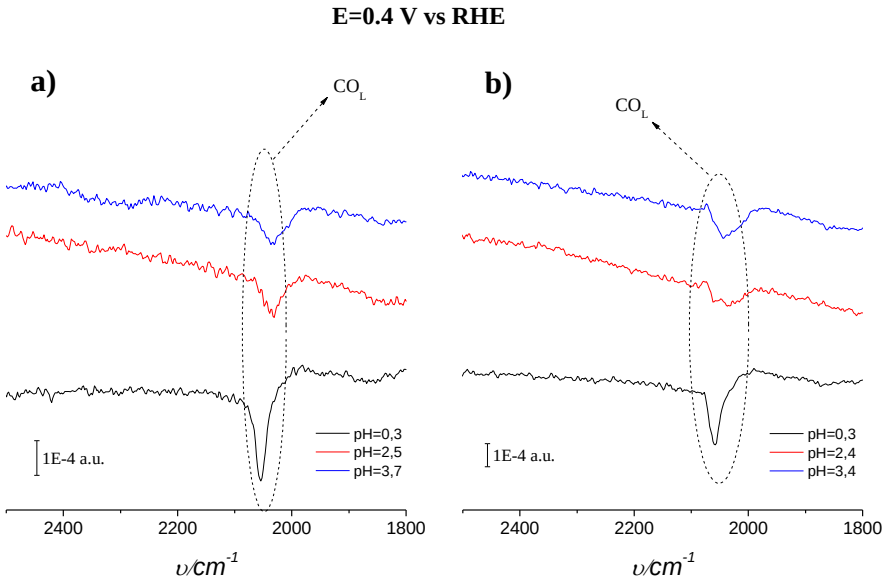

Figure 3. ATR spectra obtained at E=0.4 V vs RHE for (a) (100) Pt and (b) (111) Pt nanoparticles in 0.05 M CH_3CH_2OH + 0.5 M SO_4^{2-} at different pHs (reference spectra at 0.9 V).

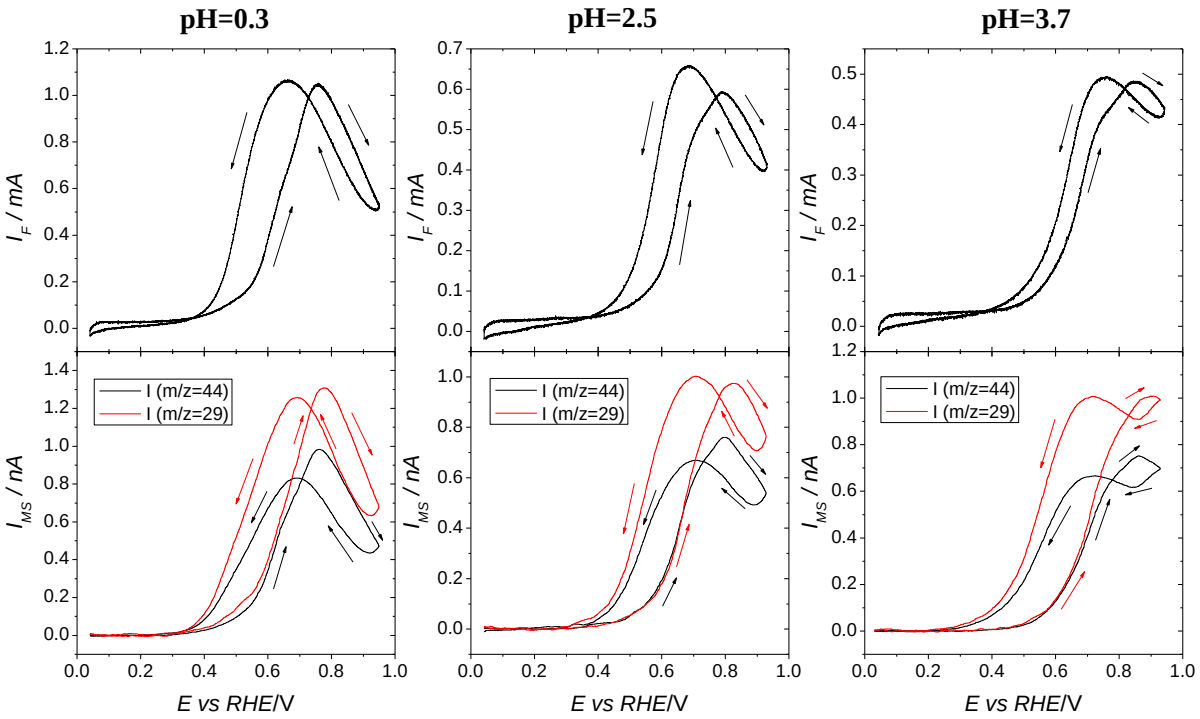

Figure 4. Cyclic voltammetry (top) and mass spectrometric cyclic voltammograms for m/z=44 and m/z=29 (bottom) for the 2nd cycle during ethanol electroxidation in 0.05 M CH_3CH_2OH + 0.5 M SO_4^{2-} on (100) Pt nanoparticles. Scan rate: 0.005 V s^{-1}.

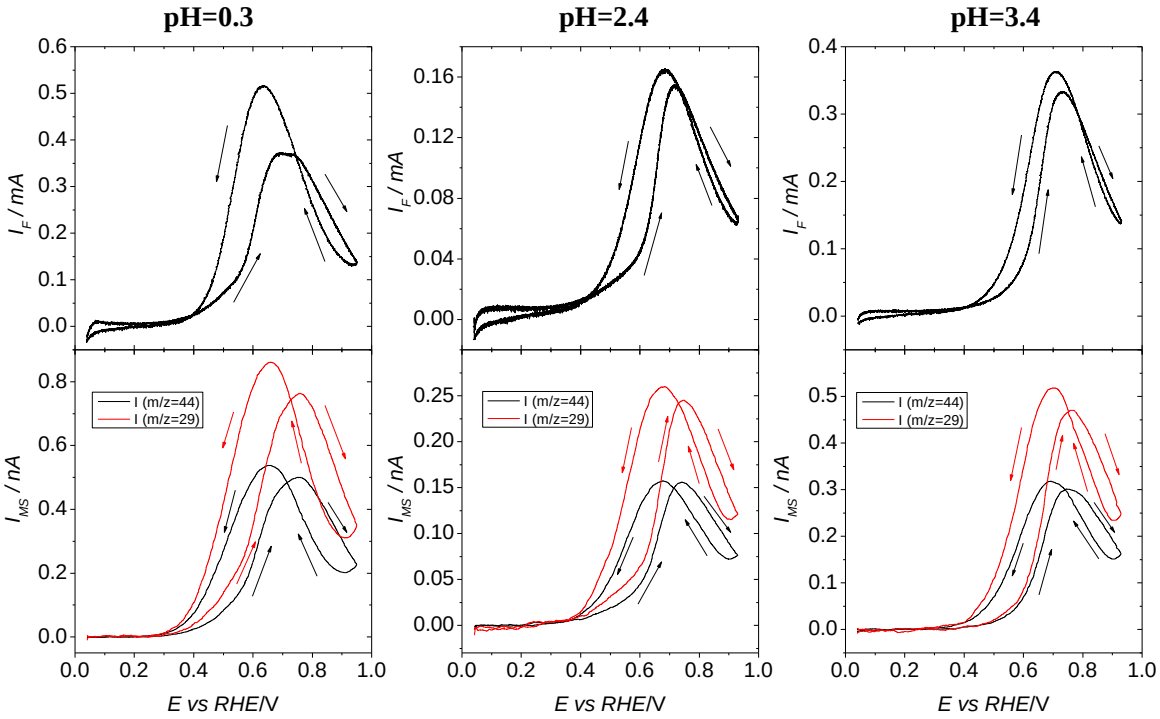

Figure 5. Cyclic voltammetry (top) and mass spectrometric cyclic voltammograms for m/z=44 and m/z=29 (bottom) for the 2nd cycle during ethanol electroxidation in 0.05 M CH_3CH_2OH + 0.5 M SO_4^{2-} on (111) Pt nanoparticles. Scan rate: 0.005 V s^{-1}.

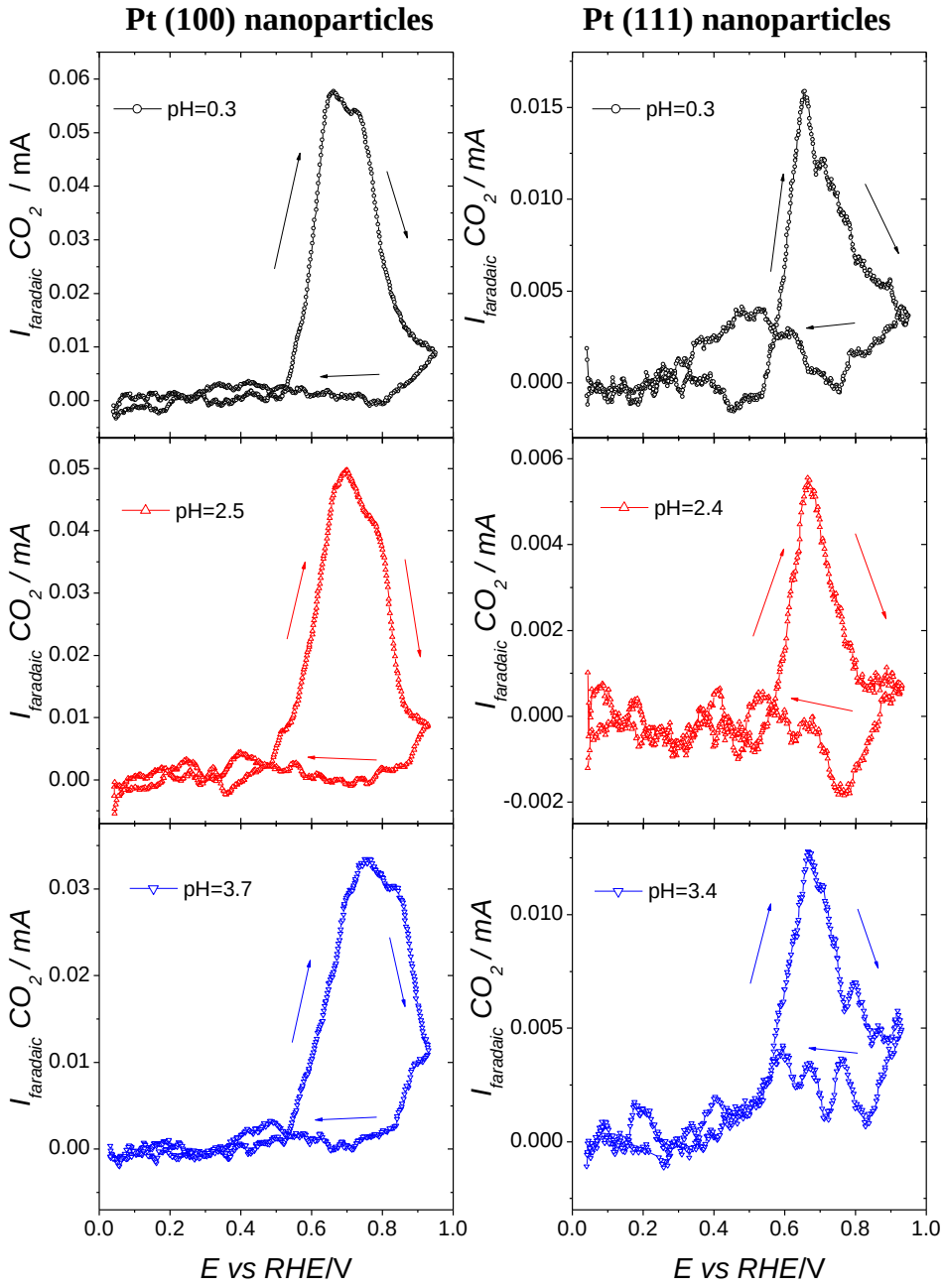

Figure 6. CO_2 formation currents using data from figures 4 and 5 for 0.05 M CH_3CH_2OH + 0.5 M SO_4^{2-} (see text for more details).

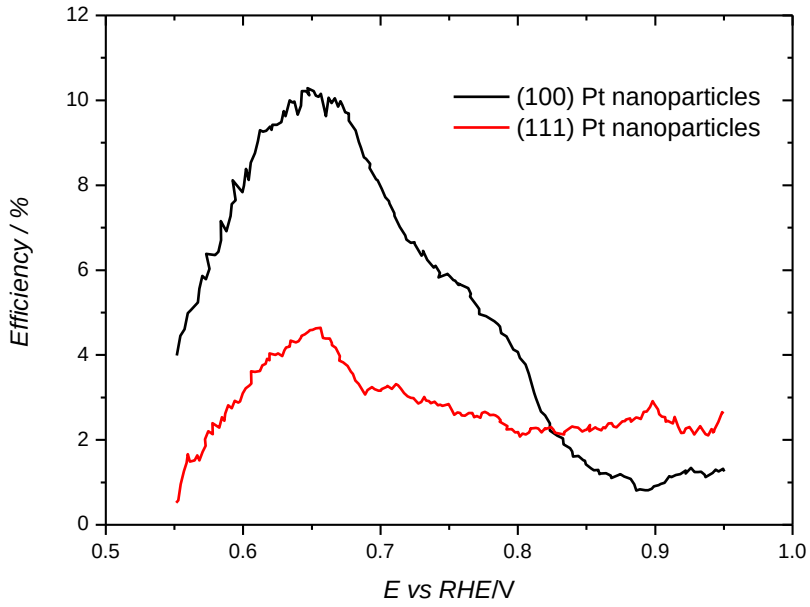

Figure 7. CO_2 current **e**fficiency vs potential for (100) Pt nanoparticles and (111) Pt nanoparticles in the ethanol oxidation reaction (0.05 M) in 0.5 M H_2SO_4 (pH=0.3).

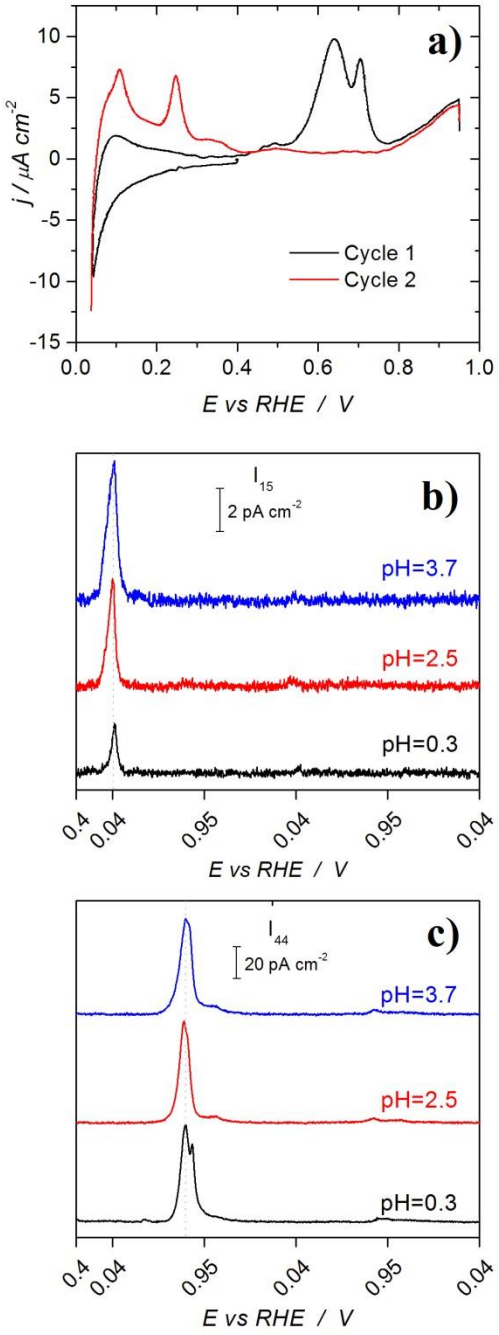

Figure 8. Ethanol stripping experiments after adsorption for 2 minutes in 0.05 M ethanol + 0.5 M SO_4^{2-} at 0.4 V vs RHE on (100) Pt nanoparticles: Voltammetric response at 0.005 V s^{-1} (a) and mass spectrometric current densities of m/z=15 (b) and m/z=44 (c).

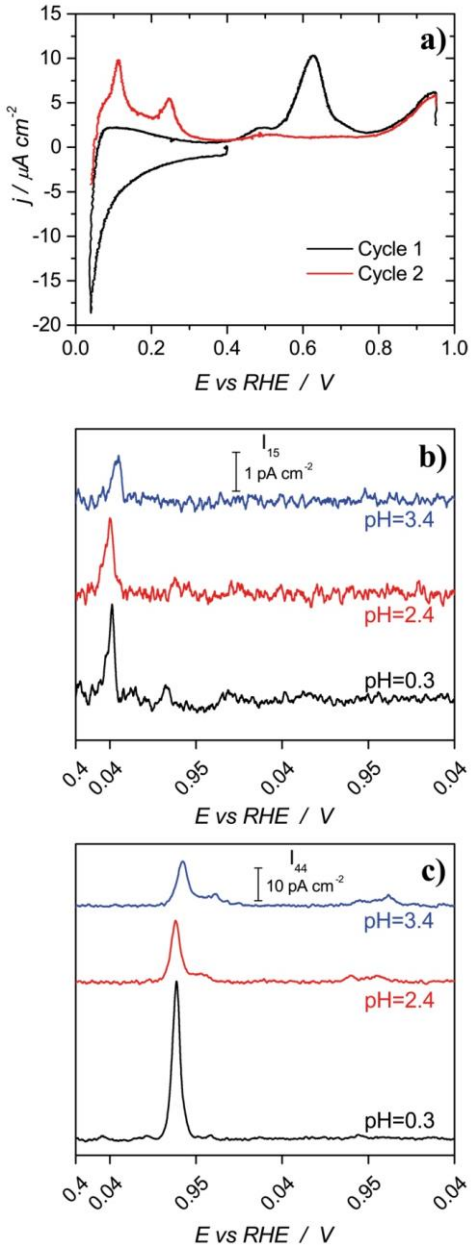

Figure 9. Ethanol stripping experiments after adsorption for 2 minutes in 0.05 M ethanol + 0.5 M SO_4^{2-} at 0.4 V vs RHE on (111) Pt nanoparticles: Voltammetric response at 0.005 V s^{-1} (a) and mass spectrometric current densities of m/z=15 (b) and m/z=44 (c).

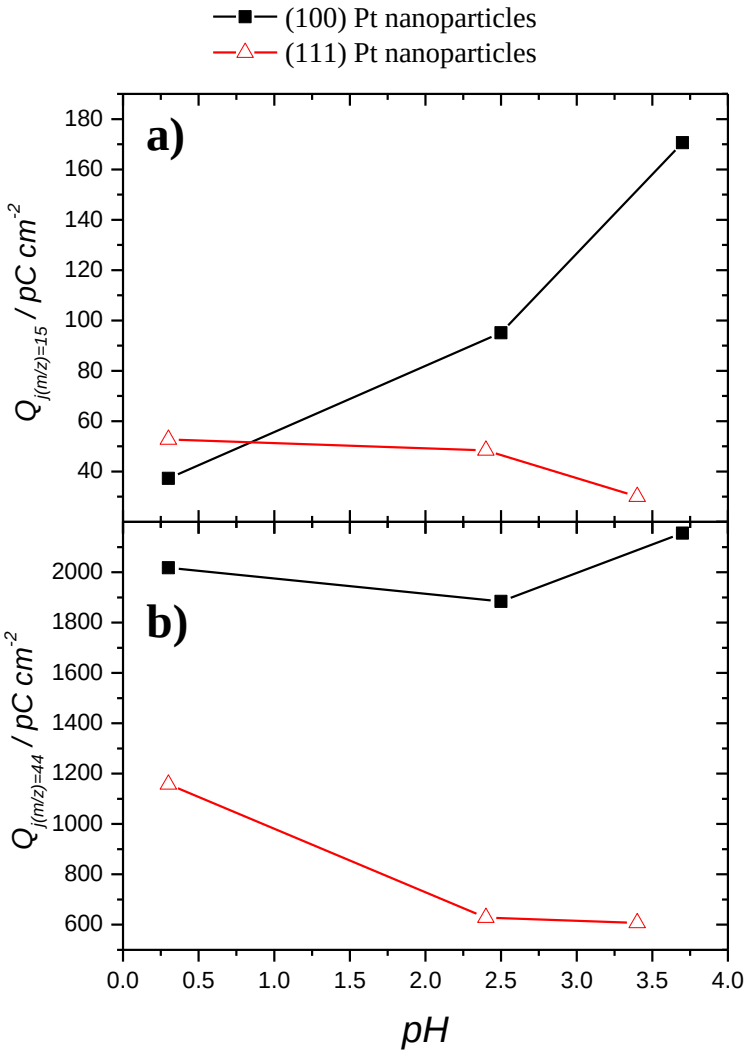

Figure 10. a) CH_x and b) CO_2 charge vs pH. Data obtained from figures 7 and 8.